Two-point momentum correlations of few ultracold quasi-one-dimensional trapped fermions: Diffraction patterns

Benedikt B. Brandt,* Constantine Yannouleas,† and Uzi Landman‡
School of Physics, Georgia Institute of Technology, Atlanta, Georgia 30332-0430, USA
(Received 21 August 2017; published 30 November 2017)

Spatial and momentum correlations are important in the analysis of the quantum states and different phases of trapped ultracold atom systems as a function of the strength of interatomic interactions. Identification and understanding of spin resolved patterns exhibited in two-point correlations, accessible directly by experiments, are key for uncovering the symmetry and structure of the many-body wave functions of the trapped system. Using the full configuration interaction method for exact diagonalization of the many-body Hamiltonian of $N = 2$–4 fermionic atoms trapped in single, double, triple, and quadruple wells, we analyze both two-point momentum and space correlations, as well as associated noise distributions, for a broad range of interparticle contact repulsion strengths and interwell separations, unveiling characteristics allowing insights into the transition, via an intermediate phase, from the noninteracting Bose-Einstein condensate to the weakly interacting quasi-Bose-Einstein regime, and from the latter to the strong-repulsion Tonks-Girardeau (TG) one. The *ab initio* numerical predictions are shown to agree well with the results of a constructed analytical model employing localized displaced Gaussian functions to represent the N fermions. The two-point momentum correlations are found to exhibit damped oscillatory diffraction behavior. This diffraction behavior develops fully for atoms trapped in a single well with strong interatomic repulsion in the TG regime, or for atoms in well-separated multiwell traps. Additionally, the two-body momentum correlation and noise distributions are found to exhibit "shortsightedness," with the main contribution coming from nearest-neighboring particles.

DOI: 10.1103/PhysRevA.96.053632

I. INTRODUCTION

Recent groundbreaking experimental progress in time-of-flight measurements is providing an abundance of information for the two-point and higher-order momentum correlations of one-dimensional (1D) systems with a large number of trapped bosons [1–12]. Such information reflects directly the nature of the correlated many-body wave function and can be used as a tool to probe theoretical models and methodologies; e.g., it has been found [11] that 1D boson systems deviate from the predictions [13] (see also Ref. [14]) of the Bogoliubov theory [15] in the quasi-Bose-Einstein condensate (QBEC) regime between the ideal-Bose gas and the strongly correlated Tonks-Girardeau (TG) regimes.

Motivated by the above developments and the experimental advances in controlling a few deterministically prepared fermions [16,17], we present exact configuration-interaction (CI) results for the two-point momentum, as well as spatial, correlations of a few ultracold fermionic atoms confined in quasi-1D single- and multiwell traps. Theoretical investigations of two-point space correlations for a few fermions (electrons) confined in semiconductor quantum dots abound; for a small sample of earlier literature, see Refs. [18–20]. Several studies of two-point space correlations have also been reported for a few trapped ultracold atoms [21–26], but the corresponding theoretical predictions for the momentum correlations, which can be directly compared to time-of-flight measurements, are still missing. (Studies of two-point momentum correlations for bosons in the TG regime are also lacking [11].)

Based on configuration-interaction (CI) calculations, this paper provides a complete range of *ab initio* two-point momentum-correlation maps (including noise distributions) for a small number N of ultracold trapped fermions, as a function of the strength g of the short-range repulsion, the total spin (S, S_z), and for both the cases of a single-well or a multiwell trap with different interwell separations. One of our main findings shows that at the Tonks-Girardeau regime the momentum correlations exhibit a signature pattern of damped diffraction (interference) oscillations associated with a typical distance scale arising from the emergent spatial particle localization in this regime. Control of the typical diffraction length is achieved by increasing the interwell separation in singly occupied multiwell traps, resulting in a larger number of visible diffraction minima. The diffraction behavior of two-point momentum correlations was reported early on by Coulson for the case of the natural H_2 molecule, aiming at gaining momentum-space insights into molecular bonding [27]. It readily lends an interpretation of the Tonks-Girardeau regime as a special limit in the context of a general unified theory of Wigner-molecule formation in finite systems with strongly repulsive interparticle interactions [18,21,22,24,25], in particular, here, ultracold Wigner molecules (UCWMs) [24,25].

The plan of the paper is as follows: We begin in Sec. II with a short description of the theoretical methodology developed and used in this work, including (i) the CI method for exact diagonalization of the many-body Hamiltonian of N optically trapped ultracold atoms (Sec. II A), (ii) *ab initio* numerical calculations of one- and two-point real-space and momentum-space correlation, and noise, functions (Sec. II B), and (iii) analytic modeling of the above-noted correlation functions, illustrated in detail for the case of two particles with a discussion of the two-particle interference pattern and correlation-map derivation (Sec. II C). In Sec. III we display

*benbra@gatech.edu
†constantine.yannouleas@physics.gatech.edu
‡uzi.landman@physics.gatech.edu

and discuss the results of our CI calculations for the following cases: (A) two fermions in a single quasi-1D well with an emphasis on the dependence on the interatomic interaction strength and the Tonks-Girardeau limit, including an illustration of the shortsightedness of the two-body momentum noise distribution, (B) two fermions in a quasi-1D double well, and (C) three fermions trapped in quasi-1D single or triple wells, with an emphasis on spin resolved, versus spin unresolved, two-point correlation maps. Section IV is devoted to comparisons between the *ab initio* CI numerically calculated two-point spin resolved (and spin unresolved) correlations in real and momentum space for two, three, and four ultracold fermionic atoms trapped in double, triple, and quadruple wells. We summarize our work in Sec. V. In the appendixes, we give explicit expressions for the analytically derived two-point correlation functions for two (including also two-point noise functions), three, and four atoms, as well as the effective Heisenberg Hamiltonians for three and four well-localized atoms. We note that, for a small number of repelling trapped particles (electrons in semiconductor quantum dots and ultracold fermions or bosons), the mapping of the microscopic many-body Hamiltonian onto spin-chain-type, effective Heisenberg Hamiltonians has been demonstrated recently and it constitutes an ongoing active area of research; for electrons in semiconductor quantum dots see Refs. [19,20], for ultracold fermions or bosons in quasi-1D traps see Refs. [24,25,28–36].

II. METHODS

A. Many-body Hamiltonian

In this paper we employ the configuration-interaction (CI) method (referred to also as exact diagonalization method) to determine the solution of the two-dimensional N-body fermionic Hamiltonian

$$H_{\rm MB} = \sum_{i=1}^{N} H(i) + \sum_{i=1}^{N}\sum_{j>i}^{N} V(\mathbf{r}_i,\mathbf{r}_j), \tag{1}$$

where $H(i)$ represents the single-particle part of the many-body Hamiltonian and $V(\mathbf{r}_i,\mathbf{r}_j)$ represents the interaction term, with $\mathbf{r}_i \equiv (x_i,y_i)$ and $\mathbf{r}_j \equiv (x_j,y_j)$ being the space coordinates of the ith and jth particle respectively. The single-particle part $H(i)$ of the Hamiltonian contains the kinetic-energy term and a single-particle external confining potential; in this paper we consider double-, triple-, and quadruple-well confinements in a linear arrangement.

The external confining potential has been extensively described in [24,25]. The relevant potential parameters for this paper are the interwell spacing d_w, which is indicated in our figures (obviously, $d_w = 0$ for a single well) and the value of ϵ_b (determining the interwell barrier height) which is taken to be 0.5 throughout the paper. Each of the parabolic confining wells is characterized by two harmonic frequencies, $\hbar\omega_x$ (along the long x axis of the well) $\ll \hbar\omega_y$ (along the y direction), resulting in a (quasi-one-dimensional) needlelike shape confinement, so that only the lowest-in-energy single-particle space orbital in the y direction is populated. In our calculations $\hbar\omega = \hbar\omega_x =$ 1 kHz, and $\hbar\omega_y = 100$ kHz (hereafter we drop for convenience the subscript x). In experimental realizations of quasi-1D (needle-shape) confinement, a similar strategy is employed, with a ratio of 10–250 between the transverse and longitudinal confining frequencies [11,16,17]. The interaction term is given by

$$V(\mathbf{r}_i,\mathbf{r}_j) = \frac{g}{\sigma^2\pi} e^{-(\mathbf{r}_i-\mathbf{r}_j)^2/\sigma^2}. \tag{2}$$

In this paper we use $\sigma = \sqrt{2}l_0/10 = 0.1833$ μm where l_0 is the harmonic oscillator length $l_0^2 = \hbar/(M_{^6\rm Li}\omega)$ with $M_{^6\rm Li} = 10\,964.90 m_e$ being the mass of ^{6}Li. The division of l_0 in the expression for σ by a factor of 10 is motivated by the need to model short-range, contactlike interactions. Any Gaussian width σ that is much smaller than the harmonic oscillator length l_0 along the x direction is suitable and yields essentially identical final results.

Common values for g in this paper are given below, in both atomic units (energy in Rydberg and length in Bohr-radius units, a_0) and in $\hbar\omega\, l_0^2$ (often used in describing experimental setups):

g (units of Ry a_0^2)	g (units of $\hbar\omega\, l_0^2$)
0.0001	0.5486
0.001	5.486
0.01	54.86

B. Configuration-interaction method, correlation functions, and noise distributions

Details of our CI methodology and the single-particle external confining potential can be found in Refs. [18,22,24,25]. A CI many-body wave function $\Phi_{\rm CI}^N$ has good total spin S and spin projection S_z quantum numbers and is specified as a superposition of Slater determinants Ψ^N built out of spin-and-space orbitals $\varphi_i(\mathbf{w})$ [$\mathbf{w} \to (\mathbf{r},\sigma)$] belonging to a given single-particle basis set; i.e.,

$$\Phi_{\rm CI}^N = \sum_J C_J \Psi_J^N. \tag{3}$$

In expansion (3), we use all the determinants that can be built out from a basis set of K single-particle spin orbitals. The number K is allowed to increase stepwise. When the result converges with respect to the number (K) of the spin orbitals in the basis, one obtains an exact diagonalization of the many-body Hamiltonian defined in Eq. (1) [37,38]; the converged CI is often termed "full CI."

Given an N-particle wave function $\Phi(\mathbf{w}_1,\mathbf{w}_2,\ldots,\mathbf{w}_N)$, the two-point real-space correlation function normalized to unity is given as

$$\mathcal{P}(\mathbf{w}_1,\mathbf{w}_1',\mathbf{w}_2,\mathbf{w}_2') = \int_{-\infty}^{\infty} \Phi^\dagger(\mathbf{w}_1',\mathbf{w}_2',\mathbf{w}_3,\ldots,\mathbf{w}_N) \times \Phi(\mathbf{w}_1,\mathbf{w}_2,\mathbf{w}_3,\ldots,\mathbf{w}_N) d\mathbf{w}_3\ldots d\mathbf{w}_N, \tag{4}$$

where $\mathbf{w}_i$ represents the space $\mathbf{r}_i$ and spin coordinate σ_i of particle i. The one-point real-space correlation function

normalized to unity is obtained as

$$\rho(\mathbf{w}_1,\mathbf{w}_1') = \int_{-\infty}^{\infty} \Phi^{\dagger}(\mathbf{w}_1',\mathbf{w}_2,\mathbf{w}_3,\ldots,\mathbf{w}_N) \times \Phi(\mathbf{w}_1,\mathbf{w}_2,\mathbf{w}_3,\ldots,\mathbf{w}_N) d\mathbf{w}_2 \ldots d\mathbf{w}_N = \int_{-\infty}^{\infty} \mathcal{P}(\mathbf{w}_1,\mathbf{w}_1',\mathbf{w}_2,\mathbf{w}_2) d\mathbf{w}_2. \quad (5)$$

We note that the physically relevant quantities for the purpose of this paper are the diagonal parts of the correlation functions. The off-diagonal parts are used as auxiliary quantities to Fourier transform from real space to momentum space and vice versa. For the two-body and one-body momentum correlation functions, the physically relevant diagonal parts are obtained via the following Fourier transforms:

$$\mathcal{G}(\mathbf{q}_1,\mathbf{q}_2) = \frac{1}{4\pi^2} \int e^{-i\mathbf{q}_1\cdot(\mathbf{w}_1-\mathbf{w}_1')} e^{-i\mathbf{q}_2\cdot(\mathbf{w}_2-\mathbf{w}_2')} \times \mathcal{P}(\mathbf{w}_1,\mathbf{w}_1',\mathbf{w}_2,\mathbf{w}_2') d\mathbf{w}_1 d\mathbf{w}_1' d\mathbf{w}_2 d\mathbf{w}_2', \quad (6)$$

and

$$\tau(\mathbf{q}) = \frac{1}{2\pi} \int_{-\infty}^{\infty} e^{-i\mathbf{q}\cdot(\mathbf{w}_1-\mathbf{w}_1')} \rho(\mathbf{w}_1,\mathbf{w}_1') d\mathbf{w}_1 d\mathbf{w}_1', \quad (7)$$

where $\mathbf{q}_i$ represents the momentum $\mathbf{k}_i$ and spin coordinate σ_i of particle i. Once one has obtained the one-point and two-point correlation functions, the calculations of noise distributions in real $\mathcal{P}_{\mathcal{N}}$ and momentum $\mathcal{G}_{\mathcal{N}}$ space are straightforward:

$$\mathcal{P}_{\mathcal{N}}(\mathbf{w}_1,\mathbf{w}_2) = \mathcal{P}(\mathbf{w}_1,\mathbf{w}_1,\mathbf{w}_2,\mathbf{w}_2) - \rho(\mathbf{w}_1,\mathbf{w}_1)\rho(\mathbf{w}_2,\mathbf{w}_2), \quad (8)$$

and

$$\mathcal{G}_{\mathcal{N}}(\mathbf{q}_1,\mathbf{q}_2) = \mathcal{G}(\mathbf{q}_1,\mathbf{q}_2) - \tau(\mathbf{q}_1)\tau(\mathbf{q}_2). \quad (9)$$

C. Analytic modeling: Two-particle interference pattern and correlation map derivation

The microscopic numerical CI evaluation of the correlation functions defined in Sec. II B are complemented by analytical expressions extracted from a simple model of localized particles represented by displaced Gaussian orbitals in the spatial Hilbert space. In this section and the Appendixes, we display such analytical modeling for two, three, and four fermions. Here we illustrate in some detail the derivation of such interference formulas for two particles, allowing a rather immediate generalization to more complex cases, like $N = 3$ and $N = 4$ particles; the analytical expressions for the noise function for $N = 2$ are given in Appendix A, and the two-point real-space and momentum-space correlation functions for $N = 3$ and $N = 4$ particles, as well as the corresponding Heisenberg model Hamiltonians, are given in Appendixes B–D. For simplicity the calculations are done here in one dimension, with the generalization to higher dimensions being rather straightforward.

This analytic modeling grasps the main physics of particle localization in the case of repulsive two-body interaction. Moreover, it offers immediate insight why the particle localization (induced by the separated wells, as well as by Wigner-molecule formation in the case of a single well) produces a characteristic signature of a damped diffraction pattern in the two-point momentum correlations. In this modeling, we assume that the spatial part of the jth particle is approximated by a displaced Gaussian function (each localized at a position d_j),

$$\psi_j(x) = \frac{1}{(2\pi)^{1/4}\sqrt{s}} \exp\left(-\frac{(x-d_j)^2}{4s^2}\right), \quad (10)$$

where s denotes the width of the Gaussian functions.

The single-particle orbital $\psi_j(k)$ in the momentum Hilbert space is given by the Fourier transform of $\psi_j(x)$, namely $\psi_j(k) = (1/\sqrt{2\pi}) \int_{-\infty}^{\infty} \psi_j(x) \exp(ikx) dx$. Performing this Fourier transform, one finds

$$\psi_j(k) = \frac{2^{1/4}\sqrt{s}}{\pi^{1/4}} \exp(-k^2 s^2) \exp(i d_j k). \quad (11)$$

Equation (11) explicitly illustrates how the displacement d_j in the real space (associated with particle localization) generates a plane-wave behavior [the factor $\exp(id_jk)$] in the momentum space. As is calculated explicitly below, in the case of several localized particles, these plane-wave factors produce interference diffraction patterns in the two-body momentum correlations that depend in general on the characteristic mutual distances $2d_{ij} = d_i - d_j$ between the particles. One of the main conclusions from the analytic modeling, however, is that these interference patterns are primarily controlled by the minimum distance $2d = d_1 - d_2$ between adjacent particles. Moreover the interference patterns do not extend in the full range of momenta $-\infty < k < \infty$, because they are damped by the damping factor $\mathcal{A}(k) = \exp(-2k^2 s^2)$ (see below) which is the square of the exponential in Eq. (11).

As a consequence, the two-point momentum correlation function (derived from the many-body wave function) focuses on properties associated with the smallest interparticle distance in the multiparticle system—that is, it provides information associated with nearest-neighbor particles. This shortsightedness suggests that information extracted from investigations of two-point momentum distributions for finite (small) numbers of particles (for which reliable many-body results can be obtained computationally, i.e., using full CI and exact Hamiltonian diagonalization as described in this work), could enhance in a significant way the understanding of properties of larger systems under similar conditions (for example, similar interparticle interaction strength) for which reliable many-body solutions are complex and often unknown (see below).

To compare the spin resolved two-body CI correlations with those derived from the analytic model, we need to guarantee that the approximate many-body wave functions of the analytic model conserved the total spin S and its projection S_z, a property that is automatically satisfied in the microscopic CI approach in the absence of energy degeneracies. In the analytic modeling, we need to construct appropriate total-spin eigenfunctions which obey the branching diagram [20,25,39] of total-spin multiplicities and other properties described in detail in Ref. [39]. For localized particles, where (as described above) the spatial part of the wave function can be approximated by the displaced Gaussian functions, the complex task of determining the appropriate total-spin components simplifies because these can be readily obtained as total-spin eigenfunctions through the exact eigenvector solutions of an effective Heisenberg

Hamiltonian [19,20,24,25,28–36]. We stress that we need to obtain here exact solutions of the Heisenberg Hamiltonian, a task that is feasible for a small number N of particles. It is pertinent also to remark explicitly that, for the purpose of this work, specifically for analyzing the properties of the two-body correlation functions (particularly in the strongly interacting highly correlated regime), use of the most familiar mean-field solutions [40], most often employed for the description of larger particle systems, will not suffice.

As mentioned earlier, we address in this section the case of two ($N = 2$) localized fermions, for which the corresponding effective Heisenberg Hamiltonian is very simple, i.e.,

$$H = J\,\mathbf{S_1}\cdot\mathbf{S_2} - \frac{J}{4}, \tag{12}$$

where $\mathbf{S_1}$ and $\mathbf{S_2}$ are spin operators and J is the coupling constant. Using the spin primitives $|\uparrow\downarrow\rangle$ and $|\downarrow\uparrow\rangle$ this Hamiltonian can be expressed in matrix form as

$$H = J\begin{pmatrix} 0 & \frac{1}{2} \\ \frac{1}{2} & 0 \end{pmatrix}, \tag{13}$$

with eigenvalues e_1, e_2 and eigenvectors v_1, v_2,

$$e_1 = -J/2, \tag{14}$$

$$e_2 = J/2, \tag{15}$$

$$v_1 = \frac{1}{\sqrt{2}}(|\uparrow\downarrow\rangle - |\downarrow\uparrow\rangle), \tag{16}$$

$$v_2 = \frac{1}{\sqrt{2}}(|\uparrow\downarrow\rangle + |\downarrow\uparrow\rangle). \tag{17}$$

Naturally, as mentioned earlier, the above Heisenberg-model solutions pertain to the spin part of the wave functions. To include the spatial component of the wave functions we need to associate each spin primitive (i.e., $|\uparrow\downarrow\rangle$ or $|\uparrow\downarrow\rangle$) with a determinant of spin orbitals $\psi_{j\sigma}(x)$ (j denotes the jth space orbital, σ represents the spin). The corresponding determinants $\mathcal{D}$'s to each primitive are

$$\begin{aligned} |\uparrow\downarrow\rangle \longrightarrow\ & \mathcal{D}_{\uparrow\downarrow}(x_1,x_2) \\ =\ & \frac{1}{\sqrt{2!}}\begin{vmatrix} \psi_{1\uparrow}(x_1) & \psi_{2\downarrow}(x_1) \\ \psi_{1\uparrow}(x_2) & \psi_{2\downarrow}(x_2) \end{vmatrix} \\ =\ & \frac{1}{\sqrt{2!}}[\psi_{1\uparrow}(x_1)\psi_{2\downarrow}(x_2) - \psi_{1\uparrow}(x_2)\psi_{2\downarrow}(x_1)], \end{aligned} \tag{18}$$

$$\begin{aligned} |\downarrow\uparrow\rangle \longrightarrow\ & \mathcal{D}_{\downarrow\uparrow}(x_1,x_2) \\ =\ & \frac{1}{\sqrt{2!}}\begin{vmatrix} \psi_{1\downarrow}(x_1) & \psi_{2\uparrow}(x_1) \\ \psi_{1\downarrow}(x_2) & \psi_{2\uparrow}(x_2) \end{vmatrix} \\ =\ & \frac{1}{\sqrt{2!}}[\psi_{1\downarrow}(x_1)\psi_{2\uparrow}(x_2) - \psi_{1\downarrow}(x_2)\psi_{2\uparrow}(x_1)]. \end{aligned} \tag{19}$$

We can use the two determinants in Eqs. (18) and (19) together with the ground-state eigenvector v_1 [Eq. (16)] to form the Heitler-London [41–43] ground-state wave function $\Phi_{\rm HL}(\mathbf{x}_1,\mathbf{x}_2)$ and the associated two-body correlation function [see Eq. (4)] $\mathcal{P}_{\rm HL}(\mathbf{x}_1,\mathbf{x}'_1,\mathbf{x}_2,\mathbf{x}'_2)$, where the boldfaced $\mathbf{x} \to (x,\sigma)$,

$$\Phi_{\rm HL}(\mathbf{x}_1,\mathbf{x}_2) = \frac{1}{\mathcal{N}_2}\frac{1}{\sqrt{2}}[\mathcal{D}_{\uparrow\downarrow}(x_1,x_2) - \mathcal{D}_{\downarrow\uparrow}(x_1,x_2)], \tag{20}$$

$$\mathcal{P}_{\rm HL}(\mathbf{x}_1,\mathbf{x}'_1,\mathbf{x}_2,\mathbf{x}'_2) = \Phi^{\dagger}_{\rm HL}(\mathbf{x}'_1,\mathbf{x}'_2)\Phi_{\rm HL}(\mathbf{x}_1,\mathbf{x}_2), \tag{21}$$

where the factor $1/\mathcal{N}_2$ normalizes the HL wave function. Specifically, $\mathcal{N}_2 = \sqrt{1+S_{12}^2}$, where S_{12} is the overlap of the two (in general nonorthogonal) localized space orbitals; see Eqs. (10) and (11) in Ref. [43].

We stress here that for the case of more than two particles the additional particle coordinates need to be integrated out to arrive at the two-point correlation function, e.g., for three particles:

$$\begin{aligned} &\mathcal{P}(\mathbf{x}_1,\mathbf{x}'_1,\mathbf{x}_2,\mathbf{x}'_2) \\ &\quad = \int_{-\infty}^{\infty} \Phi^{\dagger}_{\rm gs}(\mathbf{x}'_1,\mathbf{x}'_2,\mathbf{x}_3)\Phi_{\rm gs}(\mathbf{x}_1,\mathbf{x}_2,\mathbf{x}_3)d\mathbf{x}_3; \end{aligned} \tag{22}$$

see Refs. [44,45] for details.

To proceed further with the Fourier transform, we take the spin orbitals to have a Gaussian-function spatial part [see Eq. (10)], that is

$$\psi_{j\sigma}(x) = \psi_j(x)\sigma, \tag{23}$$

where σ denotes the up ($\uparrow$ or α) or down ($\downarrow$ or β) spin. As mentioned earlier, the physically relevant quantities are the diagonal parts of the two-point correlation function in both real and momentum space [44,45], i.e.,

$$\mathcal{P}^{N=2}_{\rm HL}(\mathbf{x}_1,\mathbf{x}_2) = \mathcal{P}_{\rm HL}(\mathbf{x}_1,\mathbf{x}_1,\mathbf{x}_2,\mathbf{x}_2), \tag{24}$$

$$\begin{aligned} \mathcal{G}^{N=2}_{\rm HL}(\mathbf{q}^x_1,\mathbf{q}^x_2) = \frac{1}{4\pi^2}\int_{-\infty}^{\infty} e^{-i\mathbf{q}^x_1\cdot(\mathbf{x}_1-\mathbf{x}'_1)}\int_{-\infty}^{\infty} e^{-i\mathbf{q}^x_2\cdot(\mathbf{x}_2-\mathbf{x}'_2)} \\ \times \mathcal{P}_{\rm HL}(\mathbf{x}_1,\mathbf{x}'_1,\mathbf{x}_2,\mathbf{x}'_2)d\mathbf{x}_1 d\mathbf{x}'_1 d\mathbf{x}_2 d\mathbf{x}'_2, \end{aligned} \tag{25}$$

where here the boldfaced $\mathbf{q}^x \to (k,\sigma)$ with k being the momentum along the x direction; the analytic modeling is performed as a strictly 1D case, unlike the quasi-1D case of the CI calculations earlier.

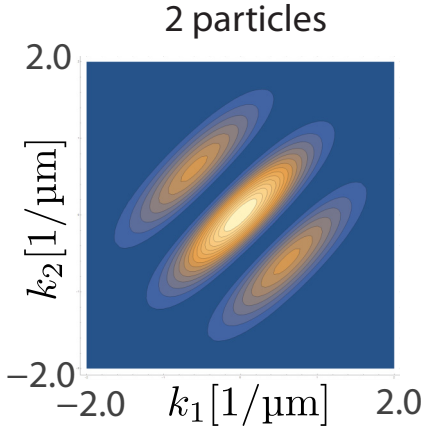

FIG. 1. Momentum correlation map for two particles separated by a distance of $2d = 4.8$ μm according to the analytic model in Sec. II C. This map was obtained by plotting Eq. (26) with k_1 on the horizontal axis and k_2 on the vertical axis. $s = 0.71$ μm.

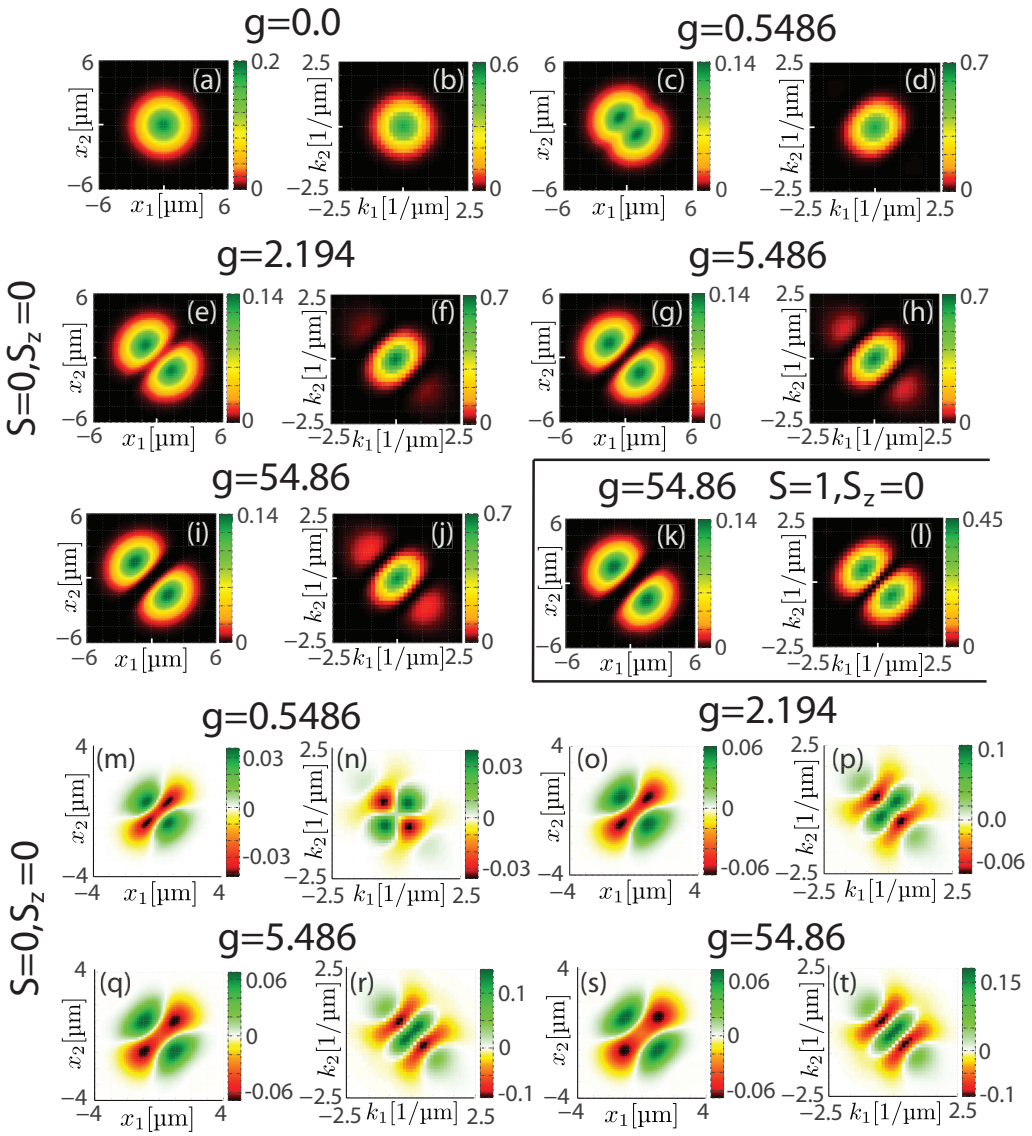

FIG. 2. Space (a),(c),(e),(g),(i),(k) and momentum (b),(d),(f),(h),(j),(l) two-point correlation maps for CI states of two ^{6}Li fermions in a single quasi-1D harmonic trap. The interatomic repulsion strength g in units of $\hbar\omega l_0^2$ is indicated in the figure. (m),(n), (o),(p), (q),(r), and (s),(t): spatial and momentum noise distributions corresponding, respectively, to the (c),(d), (e),(f), (g),(h), and (i),(j) correlation maps. Results are shown for both the ground-state singlet $S = 0$, $S_z = 0$ [(a)–(j) and (m)–(t)] and the first-excited triplet $S = 1$, $S_z = 0$ (k),(l) state. Features' amplitudes are given by the color bars on the right of each panel.

In this step it is pertinent to note that integrals over spin orbitals with different spins vanish. In order to calculate the spin resolved correlation map, we pick the terms involving the appropriate spin orbitals. For instance to calculate the correlation map with down spin for one particle and up spin for the second particle, we pick the terms involving $\uparrow^2\downarrow^2$ and $\downarrow^2\uparrow^2$ in Eqs. (24) and (25). For the spin *unresolved* correlation map, we take all spin terms into account. For two particles with the Gaussian functions centered at $d_1 = -d$ and $d_2 = d$, we obtain in this way for the spin resolved correlation map the following expression (we added the superscript $N = 2$ to denote the two-particle case illustrated here; see Appendixes B and C for $N = 3$ and $N = 4$):

$$\mathcal{G}_{\mathrm{HL}}^{N=2}(k_1\downarrow, k_2\uparrow) = \frac{4s^2 e^{-2s^2(k_1^2+k_2^2)}\cos^2[d(k_1-k_2)]}{\pi\mathcal{N}_2^2} \quad (26)$$

which agrees with results found [27] in the chemical literature for the case of the natural H_2 hydrogen molecule. An illustration of the diffractive pattern along the cross diagonal embodied in Eq. (26) is portrayed in Fig. 1. Here we wish to emphasize that the diffractive interference pattern created by the $\cos^2[d(k_1 - k_2)] \propto \{1 + \cos[(d_1 - d_2)(k_1 - k_2)]\}$ term should be an experimentally detectable signature and it is also the dominant pattern in our CI calculations (see Sec. III below). We also emphasize the presence in Eq. (26) of the cutoff prefactor $e^{-2s^2(k_1^2+k_2^2)}$, which dampens the constant-amplitude oscillatory behavior of the sinusoidal diffraction term. The expression for the spin unresolved correlation map for two particles has the same functional form as Eq. (26). This is a special property of the two opposite spin particles and for systems with more particles the spin resolved and spin unresolved expressions are in general different.

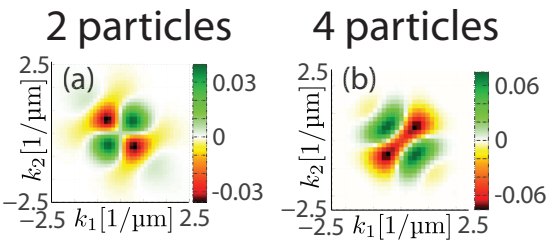

FIG. 3. Comparison of CI-calculated two-body momentum correlation map for (a) two and (b) four particles in a quasi-1D single well with $g = 0.5486\hbar\omega l_0^2$. For both system sizes, we find similar characteristic sign alternation of the momentum correlations in adjacent quadrants of the (k_1,k_2) plane, thus supporting the shortsightedness of the two-body momentum correlation map. The appearance of the negative correlations (anticorrelations) indicates deviations from the Bogoliubov theory.

Similar expressions can be derived for the case of three and four fermions in a multiwell potential (see Appendixes B and C), with the localized fermions modeled by displaced Gaussian functions. A similar diffraction pattern (with an *intrawell* interparticle distance $2d = d_1 - d_2$) develops for two repelling atoms (fermions or bosons) confined in a single well, in the TG regime (see below). When analyzing the CI results for $\mathcal{G}(\mathbf{q}_1,\mathbf{q}_2)$ below, we often make the comparison with those from the displaced-Gaussians molecular modeling.

III. CONFIGURATION-INTERACTION RESULTS

A. Two fermions in a single quasi-1D well

As mentioned earlier, we consider a short-range interparticle repulsion with a Gaussian form defined in Eq. (2). In Fig. 2 we investigate the evolution with increasing repulsion of the two-point momentum correlations [Figs. 2(b), 2(d) 2(f), 2(h), 2(j), and 2(l)] compared to the corresponding two-point real-space ones [Figs. 2(a), 2(c) 2(e), 2(g), 2(i), and 2(k)] in the case of two fermions in a single quasi-1D well. In real space we calculate the CI function $\mathcal{P}(\mathbf{w}_1,\mathbf{w}_2) = \mathcal{P}(\mathbf{w}_1,\mathbf{w}_1,\mathbf{w}_2,\mathbf{w}_2)$ [see Eq. (4)]; in momentum space we calculate $\mathcal{G}(\mathbf{q}_1,\mathbf{q}_2)$ [see Eq. (6)]. Because our system is quasi-1D (that is, needlelike shaped along the x direction due to the strong confinement in the y direction), it is natural to overlook the variation along the y direction of the trap and plot the cuts of the previous quantities at $y_1 = y_2 = 0$ and $k_1^y = k_2^y = 0$. This yields the plotted correlation maps for the position (x_1, x_2) and momentum (k_1, k_2) variables along the long x direction of the trap. The main features in these plots develop along the main diagonal (i.e., the line $x_1 = x_2$ or $k_1 = k_2$, bottom left to top right) or the cross diagonal (i.e., the line $x_1 = -x_2$ or $k_1 = -k_2$).

For the noninteracting ($g = 0$) singlet state, the two-body spatial-correlation density is azimuthally uniform having a maximum at $x_1 = x_2 = 0$ [see Fig. 2(a)]. This comes from the fermions with up and down spins occupying the same spatial $1s$ orbital of the harmonic-oscillator confinement along the x direction. However, as the strength of the interaction parameter g increases [Figs. 2(c), 2(e) 2(g), and 2(i)], two peaks along the cross diagonal develop and gradually move away from each other. This is reminiscent of the formation of a molecular dimer (like the natural H_2), often referred to as an ultracold Wigner molecule [24]. For large $g = 5.486\hbar\omega l_0^2$, a deep valley of almost zero values (black color) develops along the diagonal [Fig. 2(g)]. For very large $g = 54.86\hbar\omega l_0^2$, the separation $2d$ between the two peaks saturates and the dimer reaches the Tonks-Girardeau regime [Fig. 2(i)].

This molecule formation is reflected in the evolution of the two-point momentum correlations which follows the damped diffraction pattern [Eq. (26)] associated with a Heitler-London wave function. The diffraction pattern develops along the cross diagonal and the number of visible diffraction oscillations depends on the distance $2d$ and the spreading of the product of Gaussian functions $\mathcal{A}(k_1)\mathcal{A}(k_2)$, with $\mathcal{A}(k) \propto \exp(-2k^2s^2)$] being the square of the Fourier transform of the space orbital in Eq. (23) with $d_j = 0$. Characteristically the maximal values of the momentum correlation maps form a ridge along the main diagonal; such behavior is sometimes termed as "bunching". For smaller values of $g \leqslant 0.5486\hbar\omega l_0^2$ [Figs. 2(b) and 2(d)], the separation $2d$ is not large enough to generate secondary maxima along the cross diagonal. However, for larger values of $g \geqslant 2.194\hbar\omega l_0^2$ [Figs. 2(f), 2(h) and 2(j)], the separation $2d$ increases, and a one-oscillation (below, as well as above, the main diagonal) diffraction pattern develops which saturates at the Tonks-Girardeau limiting regime [the largest value of g

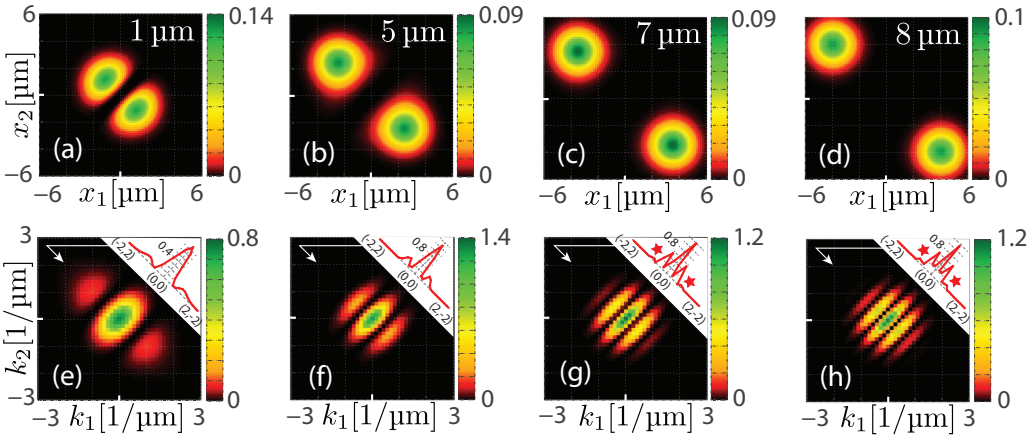

FIG. 4. Spin-resolved space (a)–(d) and momentum (e)–(h) two-point correlation maps for the CI singlet ground state (with $S = 0$, $S_z = 0$) of two ^{6}Li fermions, in quasi-1D double-well traps, with $g = 54.86\hbar\omega l_0^2$. Four different interwell separations d_w are considered. Insets in (e)–(h) display the variation as a function of k_1 along the cross-diagonal [the second diffraction peaks are marked by stars in (g),(h)].

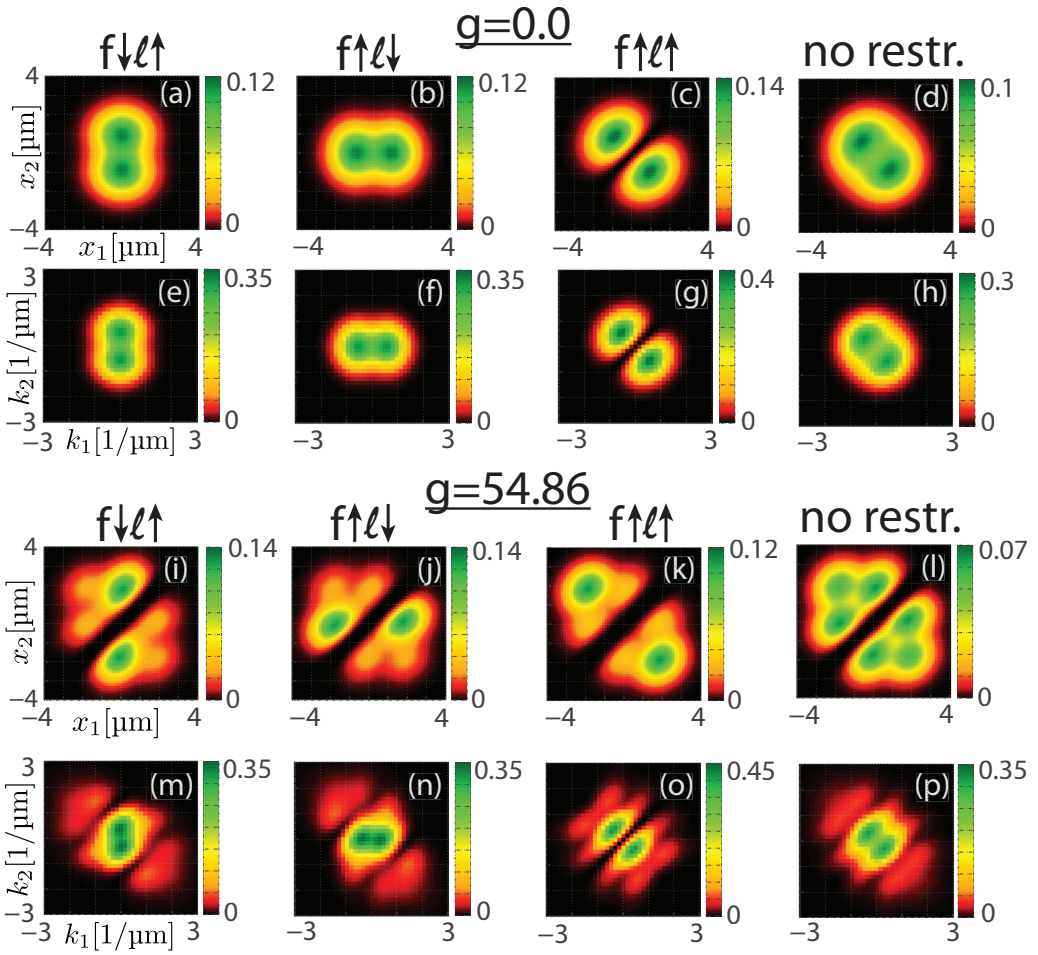

FIG. 5. Spin-resolved space (a)–(d) and (i)–(l) and momentum (e)–(h) and (m)–(p) two-point correlation maps for the CI ground state (with $S = 1/2$, $S_z = 1/2$) of three ^{6}Li fermions in a quasi-1D single-well trap; noninteracting ($g = 0$) (a)–(h) and strongly repelling ($g = 54.86\hbar\omega l_0^2$) (i)–(p). The labels $f\downarrow\ell\uparrow$, $f\uparrow\ell\downarrow$, and $f\uparrow\ell\uparrow$ indicate the spin restriction of the 2D correlation maps. (d),(h) and (l),(p) give spin unresolved maps.

considered, Fig. 2(j)]. For a single well, saturation of $2d$ with increasing g limits the number of oscillations in the diffraction pattern due to the damping factors, and a larger number of diffraction oscillations cannot be observed as $g \to \infty$.

For the triplet state, the short-range repulsion has no influence, and the correlation maps are independent of g. The g-independent real-space correlation map [Fig. 2(k)] agrees with that of the singlet UCWM state near the Tonks-Girardeau limit [large g, Fig. 2(i)], suggesting that the Pauli exclusion acts in a similar fashion as a contact repulsion with infinite strength. This is in agreement with the well-known mapping between the two-fermion singlet and triplet wave functions referred to as "fermionization," observed also experimentally [46]. The corresponding momentum correlation map for the triplet [Fig. 2(l)], however, is drastically different compared to that of the singlet state [Fig. 2(j)]. In particular, the momentum correlation map exhibits a deep trough (colored black) along the main diagonal instead of a ridge (colored green); such trough formation is sometimes termed "anti-bunching". This trough denotes a vanishing of the probability for finding two fermions with parallel spins having the same momentum, a property imposed by the Pauli principle in momentum space.

It is rewarding to note that the analytic modeling yields result in full agreement with the CI result in Fig. 2(l). Indeed

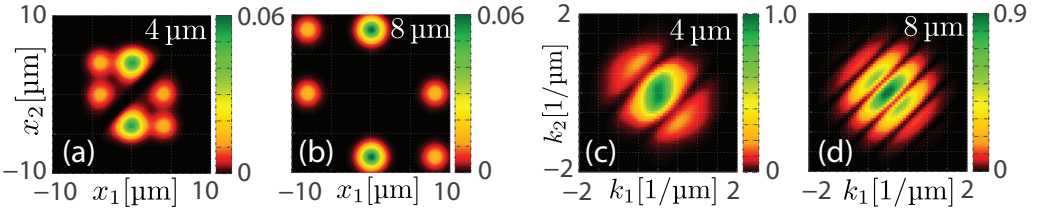

FIG. 6. Spin-resolved space (a),(b) and momentum (c),(d) two-point correlation maps for the CI ground state (with $S = 1/2$, $S_z = 1/2$) of three ^{6}Li fermions in quasi-1D triple-well traps ($g = 54.86\hbar\omega l_0^2$). Two different interwell separations d_w are considered.

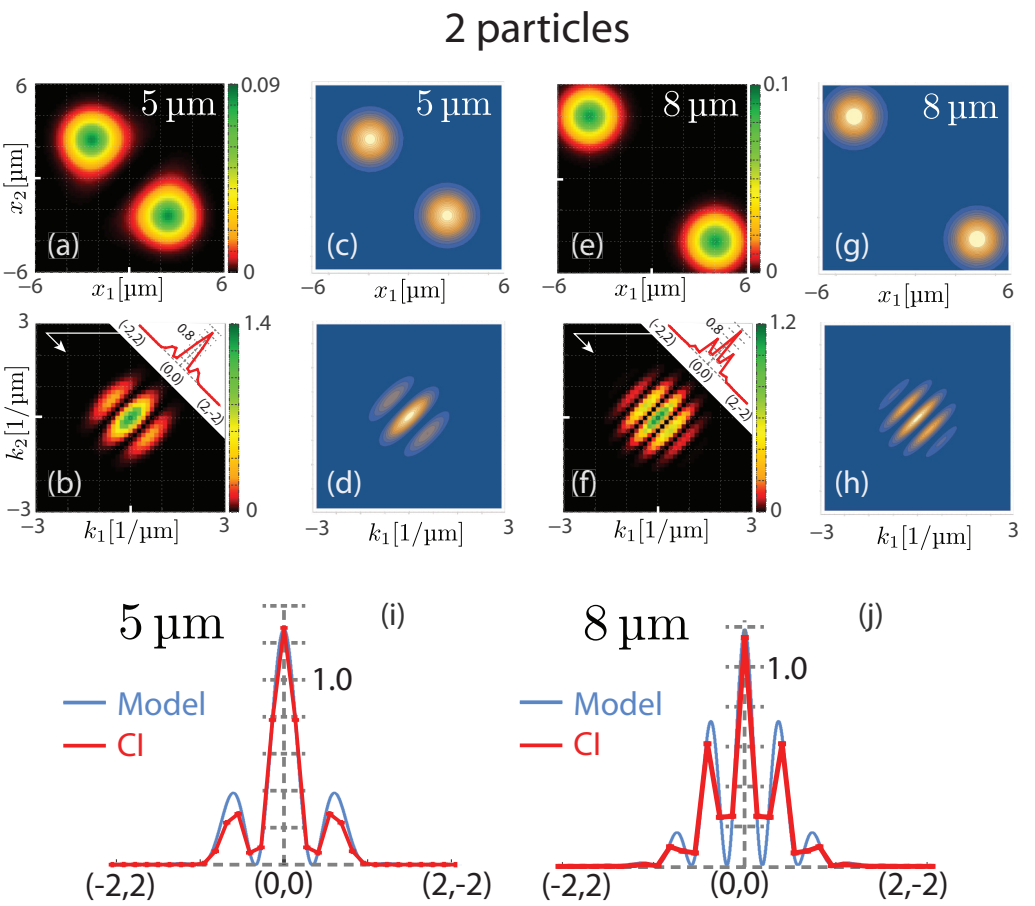

FIG. 7. Comparing the spin resolved correlation map predictions from the analytic model with the CI results calculated for the singlet ground state (with $S = 0$, $S_z = 0$) of two ^{6}Li fermions, interacting with $g = 54.86\hbar\omega l_0^2$, in a quasi-1D double-well trap (see Fig. 4). The interwell distance d_w in μm is indicated in the figure panels. The first row gives the two-point spatial correlation maps, and the second row shows the two-point momentum correlation maps. The first (a),(b) and third (e),(f) columns correspond to the CI results, and the second (c),(d) and fourth (g),(h) display the analytic results; the insets in (b) and (f) show cuts in the momentum correlation maps along the cross diagonal. In (i) and (j) we show, respectively, a cut through the cross diagonal in the CI and analytic momentum-correlation maps, calculated for $d_w = 5$ μm (b),(d), and for $d_w = 8$ μm (f),(h); the analytic results in (i) and (j) (blue curves) were matched at their maximum value to the maximum in the corresponding CI (red curves) calculated momentum correlation. In the analytic formulas, $s = 0.91$ μm for both distances $d_w = 5$ μm and $d_w = 8$ μm.

the two-body momentum correlations for the Heitler-London triplet, built out of two displaced Gaussian space orbitals (positioned at $d_1 = -d$ and $d_2 = d$), are given by

$$\mathcal{G}^{N=2}_{\mathrm{HL,t}}(k_1 \uparrow, k_2 \uparrow) \propto \frac{4s^2 e^{-2s^2(k_1^2+k_2^2)} \sin^2[d(k_1 - k_2)]}{\pi}. \quad (27)$$

It is apparent that the term $\sin^2[d(k_1 - k_2)]$ in Eq. (27) reproduces the deep trough visible in the CI correlation map [see Fig. 2(l)] along the main diagonal ($k_1 = k_2$).

From the two-point correlation maps, one may extract the often used [1,11,13] corresponding noise distributions [Figs. 2(m)–2(t)]; the two-point noise distributions are obtained by subtracting the product of the corresponding one-point momentum correlations, see Eqs. (8) and (9). These noise distributions show both positive and negative values, with the negative ones corresponding to the vanishing probability troughs in the correlation maps proper. In the case of real-space plots [Figs. 2(m), 2(o) 2(q), and 2(s)], the noise distributions again reveal the progressively increasing separation of two positive peaks (colored green) along the cross diagonal, which corresponds to the formation of a UCWM. For the momentum plots [Figs. 2(n), 2(p) 2(r), and 2(t)], it is remarkable that for the weak repulsion value $g = 0.5486\hbar\omega l_0^2$ [Fig. 2(n)], our noise distributions closely resembles the QBEC square-shaped pattern $(+,-,+,-)$ measured for a system comprised of a large number of 1D bosons [11]. For even stronger g's [Figs. 2(p), 2(r) and 2(t)], close to the TG regime, our noise maps display a more complex shape that reflects the oscillations in the corresponding diffraction pattern of the two-point momentum correlations, that is two negative areas (red color) enclosed by three positive areas (green color).

Before presenting our results for multiwell systems, we illustrate in Fig. 3 the shortsightedness of the two-body momentum correlations by comparing the two-body momentum noise maps for two [Fig. 3(a)] and four [Fig. 3(b)] particles confined in a single well, for a repulsion strength $g = 0.5486\hbar\omega l_0^2$ [see momentum noise map in Fig. 2(n)]; for additional information about the shortsightedness of the

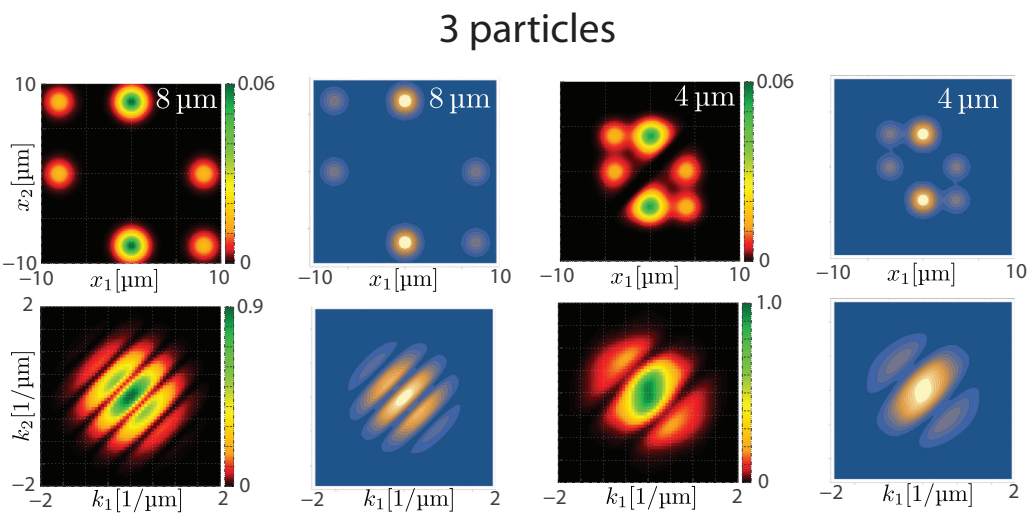

FIG. 8. Comparing the spin resolved real-space (top row) and momentum-space (bottom row) correlation-map predictions from the analytic model with the CI results calculated for the ground state (with $S = 1/2$, $S_z = 1/2$) of three ^{6}Li fermions in a quasi-1D triple-well trap with interaction strength of $g = 54.86\hbar\omega l_0^2$ (see Fig. 6). The first and third column represent the CI results, the second and fourth the analytic results. The interwell distances d_w (evenly spaced wells) are specified in the panels. In the analytic formulas, $s = 0.91$ μm for both interwell distances.

momentum correlation function, see text following Eq. (B4) in Appendix B. Comparison of the noise maps in Fig. 3, reveals that these show similar characteristic sign alternations portraying opposite-momentum correlations and anticorrelations, as predicted [7] and, more recently, observed experimentally [11]. As we noted in the Introduction, the appearance of such characteristics in the two-body momentum noise correlations is a signature of deviations from the time-honored Bogoliubov theory [7,11], whose treatment necessitates many-body theories beyond the mean-field approximation. Underlying the persistent appearance of these characteristics in few particle quasi-1D systems of variable size (see Fig. 3) is the aforementioned shortsightedness of the two-body momentum correlations.

These findings support our suggestion that investigations of few-body systems could be used to shed light on experimental observations pertaining to certain complex many-body properties (such as the effect of interparticle interactions of variable strength on the nature of quantum liquids, including deviations from the Bogoliubov theory in quasi-1D systems in the QBEC regime and for stronger repulsive interactions, that is the TG regime) even when such experiments are carried on larger systems (see, e.g., Ref. [11]).

B. Two fermions in a quasi-1D double well

To gain further insight into the trends generated through varying the separation between the two high-probability peaks

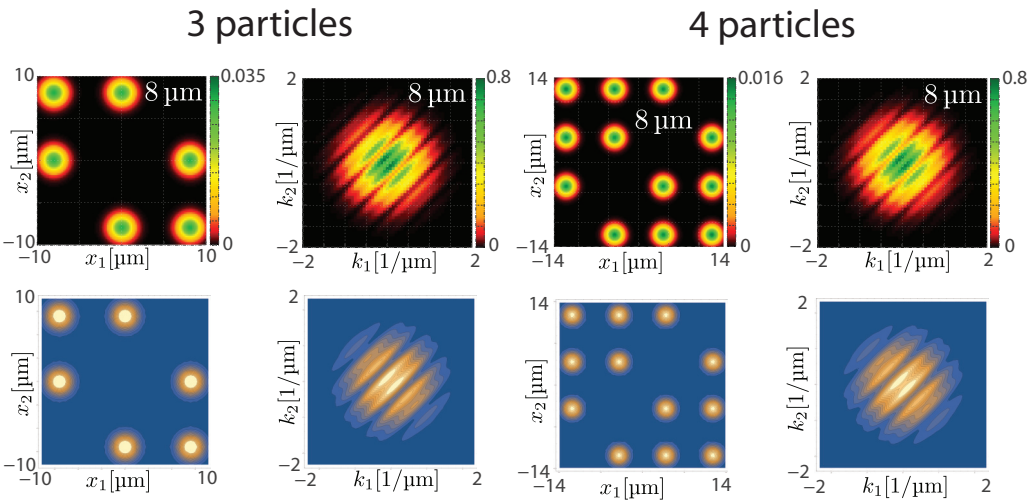

FIG. 9. Comparing the spin *unresolved* two-body correlation map predictions from the analytic model with the spin unresolved CI results for the ground state of three ^{6}Li fermions in a quasi-1D triple-well trap, and four ^{6}Li fermions in a quasi-1D quadruple-well trap, with interaction strength of $g = 54.86\hbar\omega l_0^2$. The interwell distance d_w (evenly spaced wells) in μm is indicated in the figures. The first and second columns represent the three-particle results, the third and fourth columns represent the four-particle results. The top row shows the CI results, the bottom row shows the analytic predictions. For each distance we show both the real-space correlation function (left) and the momentum-space one (right). In the analytic formulas, $s = 0.91$ μm for both the cases of three and four ^{6}Li fermions.

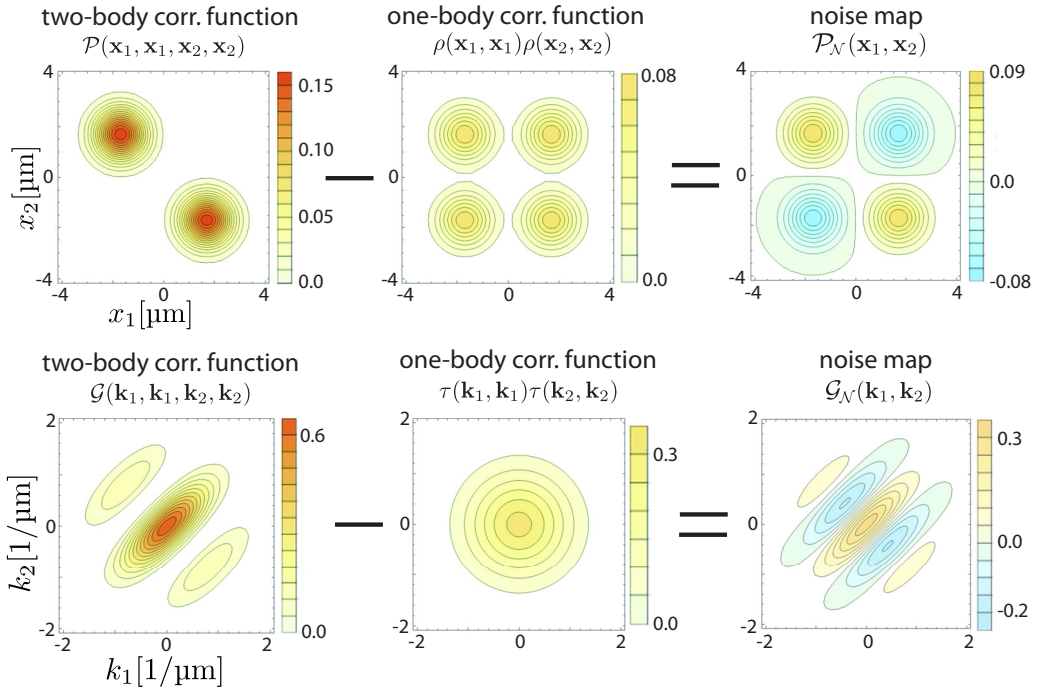

FIG. 10. Illustration of the noise-map calculation [see Eqs. (A5) and (A6)], for two particles in a single well, separated by a distance $2d = 3.4$ μm. The noise maps are obtained by subtracting the product of one-body correlation functions for the two particles from the two-body correlation function. The first row shows the real-space correlation functions and the resulting noise map after subtraction. The second row shows the same calculation in momentum space. The contour levels and the color scheme are the same throughout each row. In the analytic formulas, $s = 0.71$ μm.

in the real-space two-point correlation maps, we display in Fig. 4 spatial and momentum correlation maps for the CI singlet ground state of two ^{6}Li atoms confined in quasi-1D double-well traps at different interwell separations $d_w = 2d =$ 1, 5, 7, and 8 μm. An important observation is that the pair of maps for the smallest separation $d_w = 1$ μm [see Figs. 4(a) and 4(e)] closely resembles those of the two fermions in a single well near the Tonks-Girardeau regime [see Figs. 2(i) and 2(j)]. This further supports the interpretation of the Tonks-Girardeau regime as a special limit of the more general Wigner-molecule approach, which extends also to 2D and 3D systems [21]. As the interwell separation increases from 5 [Figs. 4(b) and 4(f)] to 7 μm [Figs. 4(c) and 4(g)] and 8 μm [Figs. 4(d) and 4(h)], an additional diffraction oscillation gradually emerges, becoming clearly visible for the separation of 8 μm.

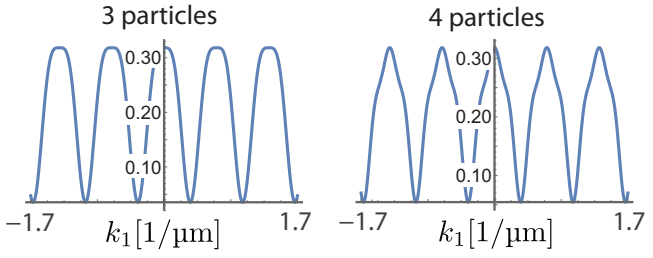

FIG. 11. Plot of the interference pattern for the fix down look up ($f\downarrow\ell\uparrow$) spin configuration for three (left) and four (right) particles. The interparticle distance (evenly spaced particles) is $2d = 4.8$ μm. The plots were obtained by plotting Eqs. (B2) and (B4) divided by the exponential term $e^{-2s^2(k_1^2+k_2^2)}$ and setting $k_2 = -k_1$; that is, these are cuts along the main cross diagonal (top left to bottom right in Fig. 12). Neither plot shows higher-order oscillations since the coefficients of the additional cosine terms are getting increasingly smaller. They therefore modify the main oscillation pattern created by the $\cos[2d(k_1 - k_2)]$, but do not show additional higher frequency oscillations. In the analytic formulas, $s = 0.71$ μm.

C. Three fermions in a quasi-1D single and triple wells

Figure 5 displays the evolution of the spatial and momentum two-point correlations for the $S = 1/2$, $S_z = 1/2$ ground state of $N = 3$ ^{6}Li atoms in a single-well trap for the noninteracting

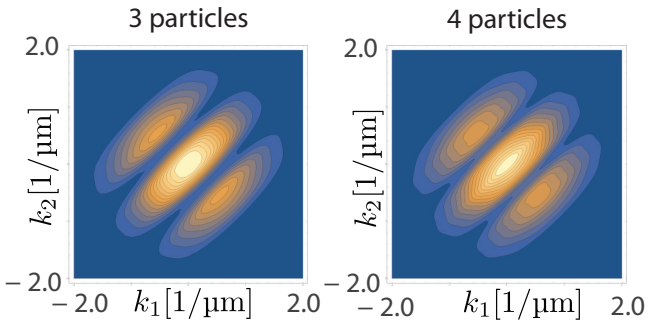

FIG. 12. Spin resolved ($f\downarrow\ell\uparrow$) two-body momentum correlation maps for three (left) and four (right) particles at a distance $2d = 4.8$ μm. The plots were obtained by plotting Eq. (B2) (left) and Eq. (B4) (right) with k_1 on the x axis and k_2 on the y axis. In this figure further oscillatory patterns beyond the ones shown are damped by the exponential factors. In the analytic formulas, $s = 0.71$ μm.

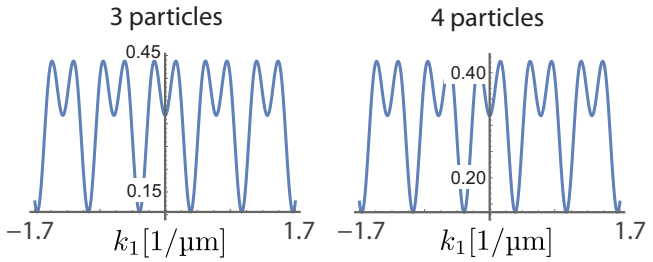

FIG. 13. Plot of the interference pattern in the spin unresolved case for three (left) and four (right) particles. The interparticle distance (evenly spaced particles) is $2d = 4.8$ μm. The plots were obtained by plotting Eqs. (C2) and (C4) divided by the exponential term $e^{-2s^2(k_1^2+k_2^2)}$. It is remarkable that the plots for three and four particles are very similar and their difference is only the overall scaling ($\sqrt{3}/2$) and a constant shift [$(6-3\sqrt{3})/(6\pi)$]. In the analytic formulas, $s = 0.71$ μm.

($g = 0$) [Figs. 5(a)–5(h)] and the strongly repelling ($g = 54.86\hbar\omega l_0^2$) case [Figs. 5(i)–5(p)]. Furthermore, both cases of spin resolved [Figs. 5(a)–5(c) and 5(e)–5(g) and Figs. 5(i)–5(k) and 5(m)–5(o)] and with no-spin restriction [Figs. 5(d) and 5(h) and Figs. 5(l) and 5(p)] are presented. In interpreting these maps, we can use the spin resolved conditional probability distribution function defined in Refs. [19,20] and in Eqs. (6) and (7) of Ref. [24]. First, we invoke the spin resolved two-point anisotropic correlation function. The spin resolved two-point anisotropic correlation function is defined as

$$P_{\sigma\sigma_f}(\mathbf{r},\mathbf{r}_f) = \langle \Phi_{\rm CI}^N | \sum_{i\neq j} \delta(\mathbf{r}-\mathbf{r}_i)\delta(\mathbf{r}_f-\mathbf{r}_j)\delta_{\sigma\sigma_i}\delta_{\sigma_f\sigma_j} | \Phi_{\rm CI}^N \rangle. \tag{28}$$

Using a normalization constant $\mathcal{N}(\sigma,\sigma_f,\mathbf{r}_f) = \int P_{\sigma\sigma_f}(\mathbf{r},\mathbf{r}_f)d\mathbf{r}$, we further define a related spin resolved conditional probability distribution (CPD) as

$$\mathcal{P}_{\sigma\sigma_f}(\mathbf{r},\mathbf{r}_f) = P_{\sigma\sigma_f}(\mathbf{r},\mathbf{r}_f)/\mathcal{N}(\sigma,\sigma_f,\mathbf{r}_f). \tag{29}$$

The label "$f\downarrow$" in "$f\downarrow\ell\uparrow$" corresponds to a selected observation ("fixed," or "f") point, with the arrow denoting the chosen spin direction at that observation point. For that selected observation (fixed) point on the x_1 (or k_1) axis, corresponding to particle "1," we search ("look for," or "ℓ") at all points along the x_2 (or k_2) axis, corresponding to particle "2," with a spin direction $\uparrow$, and record in the map the probabilities of finding particle 2 with the specified spin direction at these points. Repeating this process for all values along the x_1 axis (that is, all observation points) completes the interpretation of the label $f\downarrow\ell\uparrow$ in the correlation maps. To reiterate, the physical meaning of the notation $f\downarrow\ell\uparrow$, $f\uparrow\ell\downarrow$, $f\uparrow\ell\uparrow$ is based on the fact that a conditional probability can be extracted from the correlation maps by fixing the indices of one particle, i.e., spin and position. Indeed the cuts in the correlation maps defined by $x_1 = \text{const}$ ($k_1 = \text{const}$) portray the conditional probability of finding a second particle with predetermined spin at x_2 (k_2) assuming that the first particle with given spin is fixed at $x_1 = \text{const}$ ($k_1 = \text{const}$).

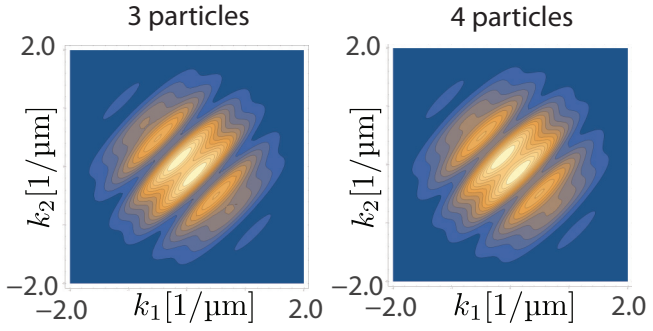

FIG. 14. Spin unresolved correlation maps for three (left) and four (right) particles at a distance $2d = 4.8$ μm (evenly spaced particles). The plots were obtained by plotting Eq. (C2) (left) and Eq. (C4) (right) with k_1 on the x axis and k_2 on the y axis. In the analytic formulas, $s = 0.71$ μm.

To facilitate understanding of the spin resolved maps in Fig. 5, we mention that for $g = 0$ the many-body configuration is $1s^2 1p$, i.e., there are two spin-up fermions occupying the $1s$ and $1p$ orbitals and one spin-down fermion occupying again the $1s$ orbital. For the strong $g = 54.86\hbar\omega l_0^2$, the appropriate spin function for a linear Wigner molecule of three localized fermions is [19] $(2|\uparrow\downarrow\uparrow\rangle - |\uparrow\uparrow\downarrow\rangle - |\downarrow\uparrow\uparrow\rangle)/\sqrt{6}$. For the noninteracting case, our CI calculations give double-peaked space and momentum correlation maps ($f\downarrow\ell\uparrow$ and $f\uparrow\ell\downarrow$) that reflect the presence of the $1p$ orbital [Figs. 5(a), 5(e) 5(b), and 5(f)]. Fixing a spin-up and looking for the other spin-up ($f\uparrow\ell\uparrow$) exhibits a valley of vanishing probabilities along the main diagonal; this is a reflection of the Pauli fermion statistics in both the space and momentum correlations [Figs. 5(c) and 5(g)]. The spin unresolved correlations [Figs. 5(d) and 5(h)] can be understood as the sum of the three spin resolved ones.

The UCWM case when $g = 54.86\hbar\omega l_0^2$ exhibits structures in real-space maps [Figs. 5(i)–5(l)] associated with the three localized fermions, i.e., a total of six peaks. For the spin resolved maps [Figs. 5(i)–5(k)], a pair of peaks is stronger, as follows from the UCWM spin function listed above (see the coefficient 2). Unlike the noninteracting case, the valleys of vanishing probabilities along the main diagonal are present for all three spin resolved maps [Figs. 5(i)–5(k)]; this is due to the fact that the three fermions do not overlap because they are well localized by the strong repulsion. The momentum maps [Figs. 5(m)–5(p)], however, are not as revealing as the space maps concerning the particle localization. Indeed, qualitatively, the main pattern in these maps is similar to that found for two fermions (see Fig. 2). Namely, there is a damped diffraction pattern along the cross diagonal exhibiting an oscillation (below, as well as above, the main diagonal) with one minimum and one secondary maximum; see pairs of narrow black troughs in Figs. 5(m), 5(n) and 5(p). This pair of troughs is less prominent for the $f\uparrow\ell\uparrow$ case [Fig. 5(o)] where a strong valley of vanishing probability develops along the main diagonal due to the Pauli exclusion principle. Naturally, there are still significant quantitative differences between the maps in Figs. 5(m)–5(p) and the maps in Fig. 2, which could be explored experimentally.

To explore further the diffraction pattern for three localized fermions, we display in Fig. 6 spin resolved ($f\downarrow\ell\uparrow$) real-space and momentum maps for three fermions in a triple-well trap for two different interwell separations $d_w = 2d = 4$ μm

and $d_w = 2d = 8$ μm in the UCWM case ($g = 54.86\hbar\omega l_0^2$). As noted earlier for two fermions, increasing the separation enhances the prominent features described in Fig. 5 for the three fermions in a single well. In particular, the patterns for the real-space correlations are enhanced versions of the pattern in Fig. 5(i). The momentum correlation map for $2d = 4$ μm [Fig. 6(c)] shows a single diffraction oscillation along the cross diagonal. However, the momentum correlation map for $2d = 8$ μm [Fig. 6(d)] shows a well-developed second diffraction oscillation, in agreement with the analytic formula of the simple model listed in Appendix B.

IV. COMPARISON OF ANALYTICAL PREDICTIONS WITH CI RESULTS

The success of the analytic modeling is evidenced by comparing analytical predictions with the *ab initio* CI numerical results. In Figs. 7–9, we compare the CI-calculated correlation maps with the correlation maps obtained from the analytical expressions (see Sec. II C and Appendixes A–C) for two, three, and four particles in double, triple, and quadruple well confinements, respectively. The agreement between both methods is excellent. We note here that the model used here (localized Gaussian functions with small overlap, and the Heisenberg Hamiltonian) becomes more complicated for smaller interwell distances. Interestingly, for the cases that we have investigated here the analytical expressions that we have derived from our model predict adequately, at least qualitatively, the features found through the microscopic CI calculations.

V. CONCLUSIONS

In this paper we have explored systematically the characteristics of spin resolved spatial and momentum-space correlations and noise distributions for two, three, and four ultracold fermionic atoms trapped in single and multiple wells; see also Appendixes A–C. These investigations aim at gaining insights into the quantum states of different phases of ultracold matter and the nature of trapped multiple-ultracold-atom moleculelike assemblies, and providing fingerprinting guidance for experiments, particularly ones with a few optically trapped, deterministically prepared and spin resolved, ultracold fermionic atoms.

Using full configuration-interaction exact-Hamiltonian diagonalization, we have evaluated and investigated two-point spatial and momentum-space correlations and noise distributions for the entire range of interatomic contact repulsions and interwell distances, exploring the transition from a noninteracting assembly to the quasi-Bose-Einstein condensate and then to the Tonks-Girardeau regime. A main result emerging from our numerical simulations using the exact many-body CI wave functions is a damped oscillatory diffraction behavior of the two-point momentum correlations and noise distributions, agreeing with our analytical model results for multiple ultracold fermionic atoms trapped in single and multiple wells.

Furthermore, the two-body momentum correlation and noise distributions are found to exhibit shortsightedness, with the main contribution coming from nearest-neighboring particles. This suggests that investigations of two-body (and possibly higher-order) momentum correlations in few-particle confined systems could be employed in the interpretation of studies carried on larger particle systems. We illustrated this approach for quasi-1D few-fermion systems with intermediate repulsive interactions which yielded two-body momentum noise correlations exhibiting opposite-momentum correlations and anticorrelations at small momenta, which closely resemble those predicted [7] and measured [11] for a system comprised of a large number of 1D bosons in the QBEC regime. These studies address deviations from the celebrated Bogoliubov theory of quantum liquids. Moreover, a more complex characteristic pattern is predicted by our calculations in the Tonks-Girardeau regime. The treatment developed here, which incorporates the effects of interatomic interactions in the two-body momentum and spatial correlations, goes beyond the Hanbury Brown and Twiss interferometry, where the free-particle statistics brings about bunching (fermions) versus anti-bunching (bosons) behavior [4,5]; in this context compare Figs. 2(j) and 2(l) for the two interacting-particles singlet and triplet states, respectively.

ACKNOWLEDGMENTS

This work has been supported by a grant from the Air Force Office of Scientific Research (USA) under Award No. FA9550-15-1-0519. Calculations were carried out at the GATECH Center for Computational Materials Science.

APPENDIX A: ANALYTIC MODELING: NOISE MAPS FOR TWO PARTICLES

To illustrate the formation of the patterns seen in the noise maps, we outline in this appendix the calculation of the noise distribution for two particles separated by a distance $2d$. The calculation of the two-body correlation function proceeds as described in Sec. II C, with the one-body correlation function obtained by applying Eq. (5), or by evaluating directly from the many-body wave function as described in Ref. [44]. We have derived the analytic expressions using the algebraic computer program *Mathematica*. In general, for the noise maps for $N = 2$ and for the two-body correlation functions for $N > 2$, these expressions are too long and complicated to be reproduced in print. For simplicity, in this appendix, and in Appendixes B and C, we present the analytic results for the case of strongly localized particles when the overlaps S_{ij} between adjacent space orbitals can be neglected—in this case, $\mathcal{N}_2 \approx 1$.

Having obtained the one- and two-body correlation functions, the noise maps can be obtained by applying Eqs. (8) and (9). Setting $d_1 = -d$ and $d_2 = d$, the needed product expressions for the one-body correlation function in real and momentum space are

$$\rho(x_1,x_1)\rho(x_2,x_2) = \mathcal{C}(s)\frac{e^{-(d+x_1)^2/2s^2}(e^{2dx_1/s^2}+1)}{2\sqrt{2\pi}s} \times \frac{e^{-(d+x_2)^2/2s^2}(e^{2dx_2/s^2}+1)}{2\sqrt{2\pi}s} \quad \text{(A1)}$$

and

$$\tau(k_1,k_1)\tau(k_2,k_2) = \mathcal{C}(s)\frac{2}{\pi}s^2 e^{-2(k_1^2+k_2^2)s^2} \quad \text{(A2)}$$

and the expressions for the two-body correlation functions are

$$\mathcal{P}^{N=2}(x_1,x_2) = \mathcal{C}(s)\frac{e^{-[2d^2+2d(x_1+x_2)+x_1^2+x_2^2]/2s^2}(e^{dx_1/s^2}+e^{dx_2/s^2})^2}{4\pi s^2}, \tag{A3}$$

$$\mathcal{G}^{N=2}(k_1,k_2) = \mathcal{C}(s)\frac{4s^2e^{-2s^2(k_1^2+k_2^2)}\cos^2[d(k_1-k_2)]}{\pi} \tag{A4}$$

which after subtraction of the one-body terms yield the desired expressions for the noise maps [see Eqs. (8) and (9)],

$$\mathcal{P}_{\mathcal{N}}^{N=2}(x_1,x_2) = \mathcal{P}^{N=2}(x_1,x_2) - \rho(x_1,x_1)\rho(x_2,x_2), \tag{A5}$$

$$\mathcal{G}_{\mathcal{N}}^{N=2}(k_1,k_2) = \mathcal{G}^{N=2}(x_1,x_2) - \tau(x_1,x_1)\tau(x_2,x_2). \tag{A6}$$

$\mathcal{C}(s)$ is an overall normalization constant (different at each one of the above formulas) whose precise value can be easily determined for a given numerical s value. The subtraction process is illustrated in Fig. 10 where we plot the real-space and -momentum correlation functions and the corresponding noise map obtained after subtraction. The resulting noise maps can be compared to Figs. 2(q) and 2(r), corresponding to the Wigner molecule case. The remaining differences in shape between the analytical and the CI noise maps originate from the spatial structure of the Wigner molecule, which is more complicated than the two separated Gaussian functions used in the analytical modeling. Nonetheless the dominant features are well reproduced. Note that all features in both the one-body and two-body correlation-function maps are positive, whereas the noise map contains patterns with opposite signs.

APPENDIX B: ANALYTIC MODELING: SPIN-RESOLVED FORMULAS ($f\downarrow\ell\uparrow$) FOR THREE AND FOUR PARTICLES

Following the derivation illustrated in Sec. II C, we may generalize it to the cases of $N = 3$ and $N = 4$ particles; see the corresponding effective Heisenberg Hamiltonians given in Appendix D. The resulting spin resolved expressions for the two-body correlations of three and four particles can be rather long, but they can be greatly simplified assuming that the Gaussian functions are equally spaced and far enough separated so that they have negligible overlap.

Here we present results for the "fixed down look up" ($f\downarrow\ell\uparrow$) spin configuration. For three Gaussians centered at $d_1 = -2d$, $d_2 = 0$, and $d_3 = 2d$ we obtain

$$\begin{aligned}\mathcal{P}_{\downarrow\uparrow}^{N=3}(x_1,x_2) = \mathcal{C}(s)\frac{e^{-[8d^2+6d(x_1+x_2)+x_1^2+x_2^2]/2s^2}}{36\pi s^2}(&-2e^{3d(x_1+x_2)/s^2}+4e^{2d(d+x_1+x_2)/s^2}+4e^{d(2d+3x_1+x_2)/s^2}+e^{d(5x_1+x_2)/s^2}+e^{d(2d+x_1+3x_2)/s^2}\\&+e^{d(2d+5x_1+3x_2)/s^2}+e^{d(x_1+5x_2)/s^2}+4e^{d(2d+3x_1+5x_2)/s^2}+4e^{2d[d+2(x_1+x_2)]/s^2})\end{aligned} \tag{B1}$$

and

$$\mathcal{G}_{\downarrow\uparrow}^{N=3}(k_1,k_2) = -\mathcal{C}(s)\frac{2s^2e^{-2s^2(k_1^2+k_2^2)}}{9\pi}(-4\cos[2d(k_1-k_2)]+\cos[4d(k_1-k_2)]-6). \tag{B2}$$

For four Gaussians centered at $d_1 = -3d$, $d_2 = -d$, $d_3 = d$, and $d_4 = 3d$ we obtain

$$\begin{aligned}\mathcal{P}_{\downarrow\uparrow}^{N=4}(x_1,x_2) = \mathcal{C}(s)\frac{e^{-(18d^2+6dx_1-6dx_2+x_1^2+x_2^2)/2s^2}}{144\pi s^2}&[(\sqrt{3}-4)(-e^{2d(2d+x_1)/s^2})+(\sqrt{3}+4)e^{4d(d+x_1)/s^2}\\&-(\sqrt{3}-4)e^{2d(2d+3x_1-2x_2)/s^2}-(\sqrt{3}-4)e^{2d(2d+2x_1-3x_2)/s^2}+4e^{3d(x_1-x_2)/s^2}+4e^{6d(x_1-x_2)/s^2}\\&+4e^{4d(2d+x_1-x_2)/s^2}+4e^{2d(4d+x_1-x_2)/s^2}-4(\sqrt{3}-1)e^{2d(2d+2x_1-x_2)/s^2}-4(\sqrt{3}-1)e^{2d(2d+x_1-2x_2)/s^2}\\&+4e^{d(8d+3x_1-3x_2)/s^2}+4(\sqrt{3}+1)e^{d(4d+5x_1-x_2)/s^2}+4(\sqrt{3}+1)e^{d(4d+x_1-5x_2)/s^2}\\&+(\sqrt{3}+4)e^{2d(2d+3x_1-x_2)/s^2}+(\sqrt{3}+4)e^{2d(2d+x_1-3x_2)/s^2}-(\sqrt{3}-4)e^{2d(2d-x_2)/s^2}\\&+(\sqrt{3}+4)e^{4d(d-x_2)/s^2}+4]\end{aligned} \tag{B3}$$

and

$$\begin{aligned}\mathcal{G}_{\downarrow\uparrow}^{N=4}(k_1,k_2) = \mathcal{C}(s)\frac{s^2e^{-2s^2(k_1^2+k_2^2)}}{9\pi}&[\cos[6d(k_1-k_2)]-2(\sqrt{3}-1)\cos[4d(k_1-k_2)]\\&+(2\sqrt{3}+3)\cos[2d(k_1-k_2)]+12].\end{aligned} \tag{B4}$$

Further support for the shortsightedness of the two-body momentum correlation is found through considerations of the analytic expression in Eq. (B4). From that expression, we find that the nearest-neighbor ($2d$ term) contribution is a dominant 72.4% of the total, compared to 16.4% and 11.2% contributions from the next-nearest-neighbor ($4d$ term) and next-next-nearest-neighbor

($6d$ term), respectively. The resulting interference patterns are illustrated in Fig. 11 (neglecting the exponential damping) and in Fig. 12.

APPENDIX C: ANALYTIC MODELING: SPIN UNRESOLVED FORMULAS FOR THREE AND FOUR PARTICLES

For the following spin unresolved expressions we restricted ourselves to the same simplifications as in the spin resolved case in the previous section. Namely the Gaussians are equally spaced and far enough apart so that their overlap can be neglected.

For three Gaussians centered at $d_1 = -2d$, $d_2 = 0$, and $d_3 = 2d$, we obtain

$$\mathcal{P}^{N=3}(x_1,x_2) = \mathcal{C}(s)\frac{e^{-[8d^2+6d(x_1+x_2)+x_1^2+x_2^2]/2s^2}}{12\pi s^2}(-2e^{3d(x_1+x_2)/s^2} + e^{2d(d+x_1+x_2)/s^2} + e^{d(2d+3x_1+x_2)/s^2} + e^{d(5x_1+x_2)/s^2} + e^{d(2d+x_1+3x_2)/s^2} + e^{d(2d+5x_1+3x_2)/s^2} + e^{d(x_1+5x_2)/s^2} + e^{d(2d+3x_1+5x_2)/s^2} + e^{2d[d+2(x_1+x_2)]/s^2}) \tag{C1}$$

and

$$\mathcal{G}^{N=3}(k_1,k_2) = \mathcal{C}(s)\frac{2s^2e^{-2s^2(k_1^2+k_2^2)}}{3\pi}\{\cos[2d(k_1-k_2)] - \cos[4d(k_1-k_2)] + 3\}. \tag{C2}$$

For four Gaussians centered at $d_1 = -3d$, $d_2 = -d$, $d_3 = d$, and $d_4 = 3d$, we obtain

$$\begin{aligned}\mathcal{P}^{N=4}(x_1,x_2) = \mathcal{C}(s)\frac{e^{-(18d^2+6dx_1-6dx_2+x_1^2+x_2^2)/2s^2}}{24\pi s^2}[&e^{4d(d+x_1)/s^2} + e^{2d(2d+x_1)/s^2} + \sqrt{3}(-e^{2d(2d+2x_1-x_2)/s^2}) \\ &+ \sqrt{3}e^{d(4d+5x_1-x_2)/s^2} - \sqrt{3}e^{2d(2d+x_1-2x_2)/s^2} + \sqrt{3}e^{d(4d+x_1-5x_2)/s^2} + e^{6d(x_1-x_2)/s^2} \\ &+ e^{4d(2d+x_1-x_2)/s^2} + e^{2d(4d+x_1-x_2)/s^2} + e^{2d(2d+3x_1-x_2)/s^2} + e^{2d(2d+3x_1-2x_2)/s^2} + e^{2d(2d+x_1-3x_2)/s^2} \\ &+ e^{2d(2d+2x_1-3x_2)/s^2} + e^{4d(d-x_2)/s^2} + e^{2d(2d-x_2)/s^2} + 1]\end{aligned} \tag{C3}$$

and

$$\mathcal{G}^{N=4}(k_1,k_2) = \mathcal{C}(s)\frac{s^2e^{-2s^2(k_1^2+k_2^2)}}{3\pi}(\sqrt{3}\cos[2d(k_1-k_2)] - \sqrt{3}\cos[4d(k_1-k_2)] + 6). \tag{C4}$$

The resulting interference patterns are plotted in Fig. 13 (neglecting the exponential damping) and Fig. 14.

APPENDIX D: EFFECTIVE HEISENBERG HAMILTONIANS AND CORRESPONDING GROUND-STATE SOLUTIONS FOR THREE AND FOUR PARTICLES

Here we give for the readers' convenience the effective Heisenberg Hamiltonians for three and four particles and their corresponding ground-state eigenvectors. We note again that, for a small number of repelling trapped particles (electrons in semiconductor quantum dots and ultracold fermions or bosons), the mapping of the microscopic many-body Hamiltonian onto spin-chain-type effective Heisenberg Hamiltonians has been demonstrated recently and it constitutes an ongoing active area of research; for electrons in semiconductor quantum dots see Refs. [19,20], for ultracold fermions or bosons in quasi-1D traps see Refs. [24,25,28–36].

The three-particle Heisenberg Hamiltonian in matrix form with spin primitives $|\uparrow\uparrow\downarrow\rangle, |\uparrow\downarrow\uparrow\rangle, |\downarrow\uparrow\uparrow\rangle$ is given as

$$H = \begin{pmatrix} 0 & J & 0 \\ J & -J & J \\ 0 & J & 0 \end{pmatrix}, \tag{D1}$$

the corresponding ground-state eigenfunction is

$$v_1 = \frac{1}{\sqrt{6}}|\uparrow\uparrow\downarrow\rangle - \sqrt{\frac{2}{3}}|\uparrow\downarrow\uparrow\rangle + \frac{1}{\sqrt{6}}|\downarrow\uparrow\uparrow\rangle. \tag{D2}$$

For four particles the Hamiltonian in matrix form with spin primitives $|\uparrow\uparrow\downarrow\downarrow\rangle, |\uparrow\downarrow\uparrow\downarrow\rangle, |\downarrow\uparrow\uparrow\downarrow\rangle, |\uparrow\downarrow\downarrow\uparrow\rangle, |\downarrow\uparrow\downarrow\uparrow\rangle, |\downarrow\downarrow\uparrow\uparrow\rangle$ is given as

$$H = \begin{pmatrix} -\frac{J_{23}}{4}+\frac{J_{12}}{2} & \frac{J_{23}}{2} & 0 & 0 & 0 & 0 \\ \frac{J_{23}}{2} & -\frac{J_{23}}{4}-\frac{J_{12}}{2} & \frac{J_{12}}{2} & \frac{J_{12}}{2} & 0 & 0 \\ 0 & \frac{J_{12}}{2} & \frac{J_{23}}{4}-\frac{J_{12}}{2} & 0 & \frac{J_{12}}{2} & 0 \\ 0 & \frac{J_{12}}{2} & 0 & \frac{J_{23}}{4}-\frac{J_{12}}{2} & \frac{J_{12}}{2} & 0 \\ 0 & 0 & \frac{J_{12}}{2} & \frac{J_{12}}{2} & -\frac{J_{23}}{4}-\frac{J_{12}}{2} & \frac{J_{23}}{2} \\ 0 & 0 & 0 & 0 & \frac{J_{23}}{2} & -\frac{J_{23}}{4}+\frac{J_{12}}{2} \end{pmatrix}, \tag{D3}$$

where we have set $J_{34} = J_{12}$ due to symmetry (we have equally spaced wells). For well-separated wells, one can further approximate $J_{12} \approx J_{23}$. Then the corresponding ground-state eigenvector is

$$v_1 = \frac{1}{\sqrt{2 + 2(1+\sqrt{3})^2 + 2(2+\sqrt{3})^2}} (|\uparrow\uparrow\downarrow\downarrow\rangle - (2+\sqrt{3})|\uparrow\downarrow\uparrow\downarrow\rangle + (1+\sqrt{3})|\downarrow\uparrow\uparrow\downarrow\rangle + (1+\sqrt{3})|\uparrow\downarrow\downarrow\uparrow\rangle - (2+\sqrt{3})|\downarrow\uparrow\downarrow\uparrow\rangle + |\downarrow\downarrow\uparrow\uparrow\rangle). \quad \text{(D4)}$$

[1] E. Altman, E. Demler, and M. D. Lukin, Probing many-body states of ultracold atoms via noise correlations, Phys. Rev. A **70**, 013603 (2004).

[2] T. Kinoshita, T. Wenger, and D. S. Weiss, Local Pair Correlations in One-Dimensional Bose Gases, Phys. Rev. Lett. **95**, 190406 (2005).

[3] M. Greiner, C. A. Regal, J. T. Stewart, and D. S. Jin, Probing Pair-Correlated Fermionic Atoms through Correlations in Atom Shot Noise, Phys. Rev. Lett. **94**, 110401 (2005).

[4] S. Fölling, F. Gerbier, A. Widera, O. Mandel, T. Gericke, and I. Bloch, Spatial quantum noise interferometry in expanding ultracold atom clouds, Nature (London) **434**, 481 (2005).

[5] T. Rom, Th. Best, D. van Oosten, U. Schneider, S. Fölling, B. Paredes, and I. Bloch, Free fermion antibunching in a degenerate atomic Fermi gas released from an optical lattice, Nature (London) **444**, 733 (2006).

[6] I. B. Spielman, W. D. Phillips, and J. V. Porto, Mott-Insulator Transition in a Two-Dimensional Atomic Bose Gas, Phys. Rev. Lett. **98**, 080404 (2007).

[7] I. Bouchoule, M. Arzamasovs, K. V. Kherunstsyan, and D. M. Gangardt, Two-body momentum correlations in a weakly interacting one-dimensional Bose gas, Phys. Rev. A **86**, 033626 (2012).

[8] A. Perrin, R. Bucker, S. Manz, T. Betz, C. Koller, T. Plisson, T. Schumm, and J. Schmiedmayer, Hanbury-Magenta and Twiss correlations across the Bose-Einstein condensation threshold, Nat. Phys. **8**, 195 (2012).

[9] R. G. Dall, A. G. Manning, S. S. Hodgman, W. RuGway, K. V. Kherunstsyan, and A. G. Truscott, Ideal n-body correlations with massive particles, Nat. Phys. **9**, 341 (2013).

[10] T. Langen, S. Erne, R. Geiger, B. Bauer, T. Schweigler, M. Kuhnert, W. Rohinger, I. E. Mazets, T. Gasenzer, and J. Schmiedmayer, Experimental observation of a generalized Gibbs ensemble, Science **348**, 207 (2015).

[11] B. Fang, A. Johnson, T. Roscilde, and I. Bouchoule, Momentum-Space Correlations of a One-Dimensional Bose Gas, Phys. Rev. Lett. **116**, 050402 (2016).

[12] S. S. Hodgman, R. I. Khakimov, R. J. Lewis-Swan, A. G. Truscott, and K. V. Kheruntsyan, Solving the Quantum Many-Body Problem via Correlations Measured with a Momentum Microscope, Phys. Rev. Lett. **118**, 240402 (2017).

[13] L. Mathey, A. Vishwanath, and E. Altman, Noise correlations in low-dimensional systems of ultracold atoms, Phys. Rev. A **79**, 013609 (2009).

[14] A. Imambekov, I. E. Mazets, D. S. Petrov, V. Gritsev, S. Manz, S. Hofferberth, T. Schumm, E. Demler, and J. Schmiedmayer, Density ripples in expanding low-dimensional gases as a probe of correlations, Phys. Rev. A **80**, 033604 (2009).

[15] N. Bogolubov, On the theory of superfluidity, J. Phys. (USSR) **11**, 23 (1947).

[16] F. Serwane, G. Zürn, T. Lompe, T. B. Ottenstein, A. N. Wenz, and S. Jochim, Deterministic Preparation of a Tunable Few-Fermion System, Science **332**, 336 (2011).

[17] S. Murmann, A. Bergschneider, V. M. Klinkhamer, G. Zürn, T. Lompe, and S. Jochim, Two Fermions in a Double Well: Exploring a Fundamental Building Block of the Hubbard Model, Phys. Rev. Lett. **114**, 080402 (2015).

[18] C. Yannouleas and U. Landman, Symmetry breaking and quantum correlations in finite systems: Studies of quantum dots and ultracold bose gases and related nuclear and chemical methods, Rep. Prog. Phys. **70**, 2067 (2007).

[19] Yuesong Li, C. Yannouleas, and U. Landman, Three-electron anisotropic quantum dots in variable magnetic fields: Exact results for excitation spectra, spin structures, and entanglement, Phys. Rev. B **76**, 245310 (2007).

[20] Ying Li, C. Yannouleas, and U. Landman, Artificial quantum-dot helium molecules: Electronic spectra, spin structures, and Heisenberg clusters, Phys. Rev. B **80**, 045326 (2009).

[21] C. Yannouleas and U. Landman, Crystalline Boson Phases in Harmonic Traps: Beyond the Gross-Pitaevskii Mean Field, Phys. Rev. Lett. **93**, 230405 (2004).

[22] L. O. Baksmaty, C. Yannouleas, and U. Landman, Rapidly rotating Boson molecules with long- or short-range repulsion: An exact diagonalization study, Phys. Rev. A **75**, 023620 (2007).

[23] M. A. García-March, B. Juliá-Díaz, G. E. Astrakharchik, Th. Busch, J. Boronat, and A. Polls, Quantum correlations and spatial localization in one-dimensional ultracold bosonic mixtures, New J. Phys. **16**, 103004 (2014).

[24] B. B. Brandt, C. Yannouleas, and U. Landman, Double-well ultracold-fermions computational microscopy: Wave-function anatomy of attractive-pairing and Wigner-molecule entanglement and natural orbitals, Nano Lett. **15**, 7105 (2015).

[25] C. Yannouleas, B. B. Brandt, and U. Landman, Ultracold few fermionic atoms in needle-shaped double wells: Spin chains and resonating spin clusters from microscopic hamiltonians emulated via antiferromagnetic Heisenberg and t-J models, New J. Phys. **18**, 073018 (2016).

[26] P. Mujal, E. Sarlé, A. Polls, and B. Juliá-Díaz, Quantum correlations and degeneracy of identical bosons in a two-dimensional harmonic trap, Phys. Rev. A **96**, 043614 (2017).

[27] C. A. Coulson, Momentum distribution in molecular systems, Part I. The single-bond, Math. Proc. Cambridge Philos. Soc. **37**, 55 (1941).

[28] A. G. Volosniev, D. V. Fedorov, A. S. Jensen, M. Valiente, and N. T. Zinner, Strongly interacting confined quantum systems in one dimension, Nat. Commun. **5**, 5300 (2014).

[29] F. Deuretzbacher, D. Becker, J. Bjerlin, S. M. Reimann, and L. Santos, Quantum magnetism without lattices in strongly interacting one-dimensional spinor gases, Phys. Rev. A **90**, 013611 (2014).

[30] A. G. Volosniev, D. Petrosyan, M. Valiente, D. V. Fedorov, A. S. Jensen, and N. T. Zinner, Engineering the dynamics of effective spin-chain models for strongly interacting atomic gases, Phys. Rev. A **91**, 023620 (2015).

[31] J. Levinsen, P. Massignan, G. M. Bruun, and M. M. Parish, Strong-coupling ansatz for the one-dimensional Fermi gas in a harmonic potential, Sci. Adv. **1**, e1500197 (2015).

[32] P. Massignan, J. Levinsen, and M. M. Parish, Magnetism in Strongly Interacting One-Dimensional Quantum Mixtures, Phys. Rev. Lett. **115**, 247202 (2015).

[33] S. Murmann, F. Deuretzbacher, G. Zürn, J. Bjerlin, S. M. Reimann, L. Santos, T. Lompe, and S. Jochim, Antiferromagnetic Heisenberg Spin Chain of a Few Cold Atoms in a One-Dimensional Trap, Phys. Rev. Lett. **115**, 215301 (2015).

[34] In particular, see the Supplemental Material in Ref. [33].

[35] L. Yang, L. Guan, and H. Pu, Strongly interacting quantum gases in one-dimensional traps, Phys. Rev. A **91**, 043634 (2015).

[36] L. Yang and X. Cui, Effective spin-chain model for strongly interacting one-dimensional atomic gases with an arbitrary spin, Phys. Rev. A **93**, 013617 (2016).

[37] A. Szabo and N. S. Ostlund, *Modern Quantum Chemistry: Introduction to Advanced Electronic Structure Theory* (McGraw-Hill, New York, 1989), Chap. 4.

[38] R. Pauncz, *Alternant Molecular Orbital Method* (Saunders, Philadelphia, 1967).

[39] R. Pauncz, *The Construction of Spin Eigenfunctions: An Exercise Book* (Kluwer/Plenum, New York, 2000).

[40] A. Auerbach, *Interacting Electrons and Quantum Magnetism* (Springer-Verlag, New York, 1994).

[41] H. Heitler and F. London, Wechselwirkung neutraler atome und homöopolare bindung nach der quantenmechanik, Z. Phys. **44**, 455 (1927).

[42] C. Yannouleas and U. Landman, Strongly correlated wave functions for artificial atoms and molecules, J. Phys.: Condens. Matter **14**, L591 (2002).

[43] C. Yannouleas and U. Landman, Magnetic-field manipulation of chemical bonding in artificial molecules, Int. J. Quantum Chem. **90**, 699 (2002).

[44] P.-O. Löwdin, Quantum theory of many-particle systems. I. Physical interpretations by means of density matrices, natural spin-orbitals, and convergence problems in the method of configurational interaction, Phys. Rev. **97**, 1474 (1955).

[45] M. Alvioli, C. Cio degli Atti, L. P. Kaptari, C. B. Mezzetti, H. Morita, and S. Scopetta, Universality of nucleon-nucleon short-range correlations: Two-nucleon momentum distributions in few-body systems, Phys. Rev. C **85**, 021001(R) (2012).

[46] G. Zürn, F. Serwane, T. Lompe, A. N. Wenz, M. G. Ries, J. E. Bohn, and S. Jochim, Fermionization of Two Distinguishable Fermions, Phys. Rev. Lett. **108**, 075303 (2012).